

Article

# The Impact of Particle Reinforcement with $\text{Al}_2\text{O}_3$ , $\text{TiB}_2$ , and $\text{TiC}$ and Severe Plastic Deformation Treatment on the Combination of Strength and Electrical Conductivity of Pure Aluminum

Ilya A. Zhukov <sup>1,2</sup>, Alexander A. Kozulin <sup>1</sup>, Anton P. Khrustalyov <sup>1,\*</sup> , Alexey E. Matveev <sup>1</sup>, Vladimir V. Platov <sup>1</sup>, Alexander B. Vorozhtsov <sup>1,2</sup>, Tatyana V. Zhukova <sup>1</sup> and Vladimir V. Promakhov <sup>1</sup>

<sup>1</sup> Faculty of Physics and Engineering, National Research Tomsk State University, Lenin av. 36, Tomsk 634050, Russia; gofra930@gmail.com (I.A.Z.); kzln2015@yandex.ru (A.A.K.); cool.mr.c@mail.ru (A.E.M.); vova.platov.85@mail.ru (V.V.P.); abv@mail.tomsknet.ru (A.B.V.); zhu-tanya@yandex.ru (T.V.Z.); vvpromakhov@mail.ru (V.V.P.)

<sup>2</sup> Institute for Problems of Chemical and Energetic Technologies of the Siberian Branch of the Russian Academy of Sciences, Socialisticheskaya st. 1, Biysk 659322, Russia

\* Correspondence: tofik0014@mail.ru; Tel.: +7-9521-555-568

Received: 18 November 2018; Accepted: 5 January 2019; Published: 11 January 2019



**Abstract:** It has been found that a high electrical conductivity of 63.1%, the International Annealed Copper Standard (IACS), and high mechanical properties are achieved by the initial aluminum alloy after undergoing four cycles of the severe plastic deformation (SPD) process. It has been found that when  $\text{TiB}_2$  particles are introduced into aluminum and the samples are subject to SPD, the mechanical characteristics of the aluminum alloy are improved. Microhardness (HV) increases from 329 to 665 MPa, yield strength (YS) increases from 38 to 103 MPa, and ultimate tensile strength (UTS) increases from 73 to 165 MPa while maintaining the initial electrical conductivity of cast aluminum without reinforcing particles (53.9–54.1% IACS).

**Keywords:** aluminum; particles; master alloy; deformation treatment; electric conductivity; mechanical properties

## 1. Introduction

Aluminum has a high application value for conductors of different types [1–3]. Pure aluminum without impure metals dissolved in its crystal lattice has the electrical conductivity of 65% IACS. This is because there are no obstacles for the free pass/scattering of electrons in aluminum crystals. Foreign inclusions, defects and atoms of other metals dissolved in the lattice could become such obstacles [4]. Meanwhile, high mechanical properties of aluminum alloys are mainly achieved by applying mechanisms involving solid-solution strengthening and subsequent accelerated aging. This includes the particle-strengthening of aluminum alloys with intermetallic phases such as Al–Sc, Al–Zr, and Al–Cu [5–7]. This means that high electrical conductivity and high mechanical properties are mutually exclusive. Due to its poor mechanical properties, pure aluminum is not used in the manufacturing of conductive elements. Alloys with a small content of alloying elements are used instead for both their mechanical properties and electrical conductivity to be acceptable [4,8,9]. It is also known that using the Al–B alloy for reinforcing aluminum [10] allows for improving electrical conductivity. This is because boron is active toward mixtures dissolved in the aluminum lattice and it escapes beyond the boundaries of the grains in the form of borides, thus allowing for the

free pass of electrons in the crystal. Another approach to increasing electrical conductivity and mechanical properties are severe plastic deformation (SPD) methods [11]. In References [4,9], it has been shown that grinding grains to submicron sizes using SPD produces ultra-fine alloys of aluminum with nanosize inclusions that exhibit excellent strength, thanks to grain-boundary and particle reinforcement. The authors have shown that SPD leads to a very low content of dissolved atoms and the absence of Guinier–Preston zones in the aluminum crystals, which significantly increases electrical conductivity [4].

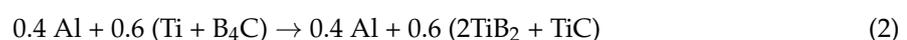
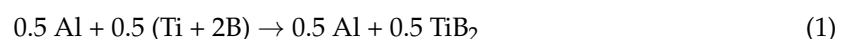
An alternative approach to increasing the mechanical properties of aluminum alloys lies in the ex situ introduction of a small amount (up to 0.1–0.2 wt.%) of nano- and micro-size neutral hard-melting particles, such as Al<sub>2</sub>O<sub>3</sub>, TiB<sub>2</sub> and SiC. This allows for a significant increase in the mechanical properties of aluminum alloys, including hardness, yield strength, tensile strength, and plasticity [12–14]. This is because when ceramic particles are introduced into the melt, they become crystallization centers and lead to the formation of a fine-grain structure of ingots. This, in turn, improves mechanical properties in accordance with the Hall–Petch relationship. Also, the strengthening is achieved via the Orowan mechanism since ceramic particles are an obstacle to the travel of dislocations [15]. The mechanical properties of the aluminum composites are rather fully studied in References [12–16]. Valiev R.Z. et al. [4,9] studied the effect of SPD on the electrical conductivity of dispersion-hardening alloys by intermetallic inclusions. The issue of the influence of ceramic inclusions (especially at nanosize scale) introduced by the “ex-situ” method on the combination of mechanical properties and electrical conductivity of aluminum remains understudied. At the same time, there are no data on the effect of SPD on the physico-mechanical properties of aluminum alloys hardened by ceramic particles. Thus, the goal of this research is to study the influence of nanosized Al<sub>2</sub>O<sub>3</sub> particles, sub-microsized TiB<sub>2</sub> and TiC particles, and deformation treatment on the mechanical properties and electrical conductivity of pure aluminum.

## 2. Materials and Methods

### 2.1. Reinforcing Particles

In the present research, three types of reinforcing particles were injected into the aluminum melt: (1) master alloys containing TiB<sub>2</sub> and TiC particles, with an average particle size of 0.9 μm; (2) master alloys containing TiB<sub>2</sub> particles, with an average particle size of 0.7 μm; and (3) Al<sub>2</sub>O<sub>3</sub> nanopowder, with an average particle size of 80 nm. The average size of agglomerates of the nanosize particles was 1.2 μm.

Master alloys containing carbide and boride particles were obtained through self-propagating high-temperature synthesis (SHS) [17,18]. To obtain SHS materials from Al–Ti–B/B<sub>4</sub>C powder systems, stoichiometric mixtures of titanium and boron/boron carbide powders were used, with the addition of aluminum powder to the stoichiometric mixtures. The weight ratio of the initial components of the charge Al–Ti–B /B<sub>4</sub>C for each experiment was selected based on the conditions of the synthesis reaction in the stationary layer-by-layer burning mode without attenuation. It was assumed that aluminum powder does not react in the charge and serves as a diluent that lowers the temperature of combustion. This, in turn, allows for the obtainment of smaller ceramic particles of TiB<sub>2</sub> and TiC by inhibiting the recrystallization process. Therefore, the calculated/theoretical/estimated reactions occurring in the SHS process for each system are presented as follows.



Titanium and boron powders, as well as titanium and boron carbide powders, were mixed in the following stoichiometric ratios: 69 wt.% Ti + 31 wt.% B and 72 wt.% Ti + 28 wt.% B<sub>4</sub>C, respectively. Next, aluminum powder was added to the stoichiometric mixture, with an amount of 50 wt.% for

the Ti + 2B system and 40 wt.% for the Ti + B<sub>4</sub>C system. The SHS process consisted of the following steps. First, there was the mixing powders, followed by pressing and setting the resulting compact into a SHS reactor. This was further followed by vacuuming, filling the working space with argon, and local combustion initiation by heating the nichrome loop in contact with the pressing surface. The methodology of the experiment, data on starting materials and equipment, and data on the structure and phase composition of the master-alloys obtained by the SHS method and used in this work are described in more detail in Reference [18].

The initial nanosized powders of aluminum oxide were produced using plasma chemical synthesis on the respective reactor units. The unit schematics, the production method and the theoretical and experimental research for optimizing the particle size distribution and morphology of the obtained powders are provided in Reference [12,16,19–21]. For powder synthesis, an initial water solution (30 wt.%) of aluminum salt Al(NO<sub>3</sub>)<sub>3</sub>·9H<sub>2</sub>O was used. The process of salt decomposition into aluminum oxide in the plasma-chemical reactor is as follows. First, salt thermolysis takes place when it is heated over 135 °C. Here, the Al(OH)<sub>2</sub>NO<sub>3</sub>·1.5H<sub>2</sub>O basic salt is formed. At higher temperatures (over 200 °C), the salt is decomposed into aluminum oxide in accordance with the following reaction.



## 2.2. Obtaining the Alloys

Industrial grade 99.5% aluminum was used as the initial material, while the rest comprised of 0.2% of Si, 0.2% of Fe, 0.1% of and Ti. Nanosized Al<sub>2</sub>O<sub>3</sub> particles and SHS master alloys were injected using a mechanical mixer. A description of the mechanical mixer and the method of particle injection into the melt are provided in Reference [13]. The melt temperature when the alloy was poured into the crystallizer was 720 °C, and the amount of injected TiB<sub>2</sub>, TiB<sub>2</sub>/TiC, and Al<sub>2</sub>O<sub>3</sub> particles were 0.1 wt.%. Under similar conditions, the reference alloy for comparison was obtained. Prismatic work pieces (8 × 8 × 45 mm<sup>3</sup>) for deformation treatment and subsequent studies were cut from the centerpieces of cylindrical casts along the principal axis. The prismatic work pieces were subjected to SPD, namely, equal-channel angular pressing (ECAP) in ad-hoc fabricated die-molds with two channels crossing at the angle of 90°. The pressing of the work pieces was repeated for two and four cycles via route Bc: turning the sample at 90° during each cycle with a temperature of 200 °C and pressing speed of 15 mm/min using a high-temperature lubricant based on molybdenum disulfide. The selected pressing procedure was supposed to be beneficial for developing an equiaxial ultra-fine structure and ensuring the isotropy of the mechanical properties throughout the material's volume. As a result of using the selected pressing method, the maximum degree of true strain in the central part of the work pieces was 2.3 for two cycles and 4.6 for four cycles. To process the work pieces from the researched alloys, a universal servohydraulic testing system (INSTRON 8801, Instron European Headquarters, High Wycombe, UK) equipped with a heating chamber was used. This equipment enabled us to maintain the required temperature, precisely adjust the pressing speed, and load up to 50 kN with an error margin of up to 0.2%. The schematics of the ECAP process are provided in Reference [22].

## 2.3. Research

Specific electrical impedance (Ω) of the alloys was measured on a unit with the precision of 0.0001 Ohm × m. From the obtained data, the specific electrical conductivity or ω (S/m) and electrical conductivity according to the International Annealed Copper Standard (IACS) were calculated.

The Vickers microhardness (HV) measurements were conducted according to ISO 6507-1:2018 "Metallic materials Vickers hardness test Part 1: Test method" on a lateral surface of the prismatic specimens in different regions along the pressing axis using the HMV G21ST Shimadzu microhardness tester (Shimadzu, Tsukinowa, Japan). These measurements were taken under a load of 0.5 N and a dwell time of 10 s. About 20 measurements were made for each specimen. The specimens' surfaces

were prepared with a standard procedure using mechanical polishing (surface finish roughness  $R_z = 0.1 \mu\text{m}$  and  $R_a = 0.025 \mu\text{m}$ ).

The microsized samples for elongation—shaped as flat double-sided blades with working parts with a size of 10 mm, thickness of 1 mm, width of 3 mm, and rounding radius of 2.5 mm—were cut from prismatic work pieces along the pressing axis using electrical discharge machining. Single-axis elongation tests were performed on a universal electromechanical testing machine, i.e., Instron 3369 (Instron European Headquarters, High Wycombe, UK), at a deformation rate of  $0.001 \text{ s}^{-1}$ , which corresponds to a tensile rate of 0.6 mm/min and a temperature of  $25 \text{ }^\circ\text{C}$ . X-ray diffraction analysis was performed using a Shimadzu XRD 6000 diffractometer (Shimadzu, Tsukinowa, Japan). on  $\text{CuK}_\alpha$  radiation, an accelerating voltage of 30 kV, and the Powder Diffraction file database and POWDER CELL 2.4 full-profile analysis software. The initial structure of the powders and the fabricated materials were researched using scanning electron microscopy with a Quanta 200™ 3D microscope (FEI Company, Thermo Fisher Scientific, Waltham, MA, USA). The particle size of the powders was measured on ANALYSETTE 22 MicroTec plus (FRITSCH, Gamburg, Germany).

### 3. Results and Discussion

#### 3.1. Master Alloys Obtained in the SHS Mode

A typical structure of the obtained SHS composites containing diboride and titanium carbide particles is provided in Figure 1. The phase compositions of the SHS master alloys obtained are provided in Table 1.

**Table 1.** The data of the phase analysis of SHS master alloys containing  $\text{TiB}_2$  and  $\text{TiC}$  particles.

Master-Alloy	Phases Detected in the Alloyage	Phase Content (wt.%)	Lattice Parameters ( $\text{Å}$ )	CSR Size (nm)	$\Delta d/d \times 10^{-3}$
(2)	$\text{TiB}_2$	57	a = 3.0336 c = 3.2327	45	0.1
	$\text{TiAl}$	43	a = 4.0620 c = 4.0456	–	–
(1)	$\text{TiB}_2$	42	a = 3.0238 c = 3.2208	41	1.7
	Al	36	a = 4.0472	46	0.5
	TiC	22	a = 4.3184	64	0.4

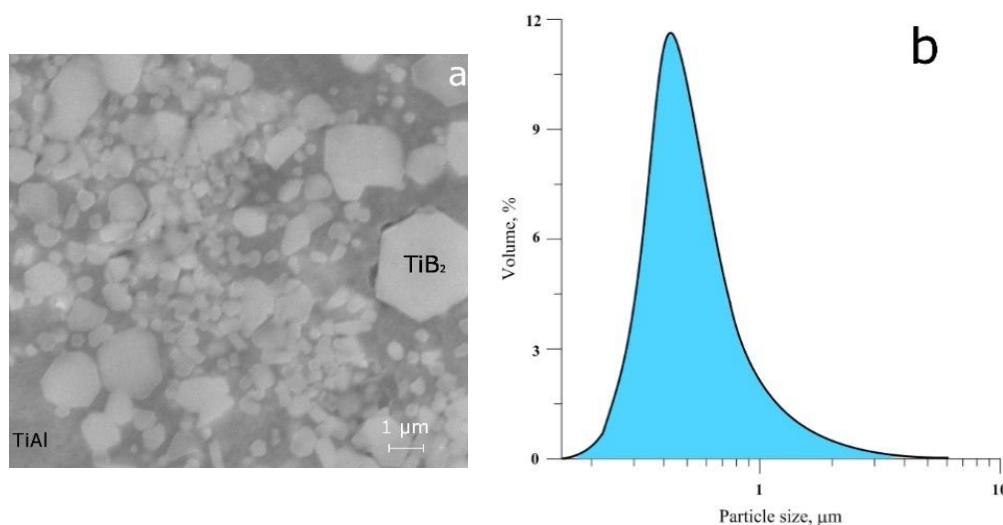


**Figure 1.** Cont.

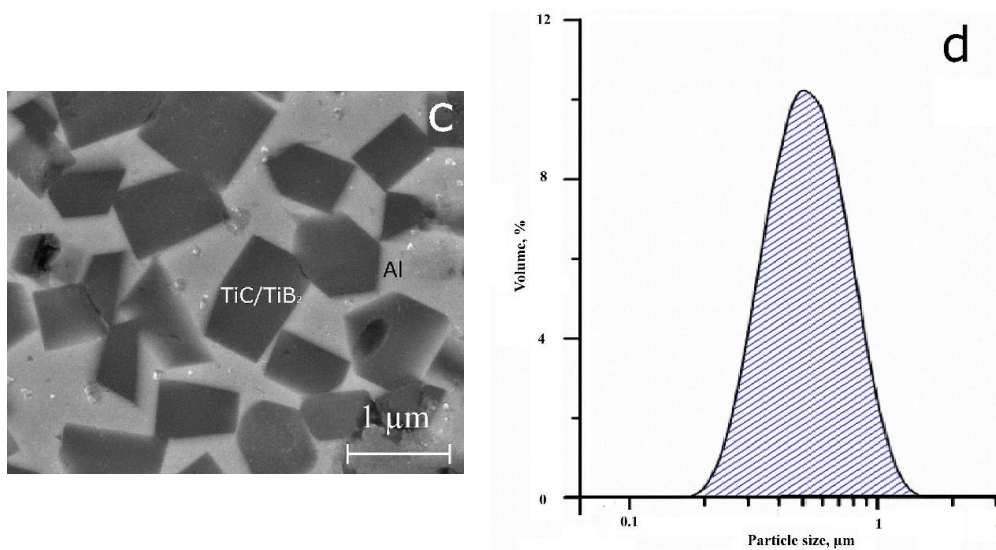


**Figure 1.** (a) The microstructure of the master-alloy 2 SHS composite containing TiB<sub>2</sub> particles. (b) Histogram of the ceramic particle distribution (TiB<sub>2</sub>) by size. (c) Master-alloy 1 SHS composite containing TiB<sub>2</sub>/TiC particles. (d) Histogram of the ceramic particle distribution (TiB<sub>2</sub>/TiC) by size.

During the SHS process, titanium carbide and boride particles form in the process of the exothermic combustion reaction (in situ) of the pressed powder systems in the sample layer via the solid phase particle diffusion mechanism involving B/B<sub>4</sub>C particles and Ti particles. The synthesis processes are accompanied by an increase in the temperature and heat emission that initiates synthesis in the next layer. This is why the weight content of the aluminum powder in the initial Al–Ti–B/B<sub>4</sub>C mix was determined experimentally, judging from the possibility of the SHS process occurring in the systems in question. Thus, it was found that the maximum possible weight content of aluminum in the mix for the stationary combustion condition at the initial sample temperature of 20 °C was over 40 wt.% for the Al–Ti–B<sub>4</sub>C system and 50 wt.% for the Al–Ti–B system. It must be noted that aluminum powder in the initial mix works not only as a matrix for the composites but also as an inert diluent that reduces the adiabatic temperature of the reaction of the Al–Ti–B<sub>4</sub>C system from 2500 °C (for Ti–B<sub>4</sub>C) to 1500 °C (Al–Ti–B<sub>4</sub>C) and the rate of the reaction from 90 to 18 mm/s. In turn, reduced combustion parameters slow down both the growth of ceramic particles of titanium diboride and carbide and the re-crystallization of these particles in the sample. Therefore, if the content of aluminum in the mix is below 40 wt.% for Al–Ti–B<sub>4</sub>C (or 50 wt.% for Al–Ti–B), then the adiabatic temperature and reaction rate are increased, and this promotes the growth of TiB<sub>2</sub>/TiC particles in the SHS composites produced.

### 3.2. Nanosize Al<sub>2</sub>O<sub>3</sub> Powder

The phase composition of the obtained Al<sub>2</sub>O<sub>3</sub> powder is represented by  $\theta$ -Al<sub>2</sub>O<sub>3</sub> and  $\gamma$ -Al<sub>2</sub>O<sub>3</sub> for 42 wt.% and 58 wt.%, respectively, in Figure 2. A SEM image and a particle size distribution histogram are provided in Figure 3. It is evident from Figure 3a that the powder includes agglomerates of nanosized particles of near-spherical morphology, and the average particle size of individual particles was 80 nm (see Supplementary Figure S1). Apparently, the agglomeration of nanoparticles takes place because of the Van der Waals forces [23], and this leads to the formation of conglomerates that affect the size distribution histograms (Figure 3b).

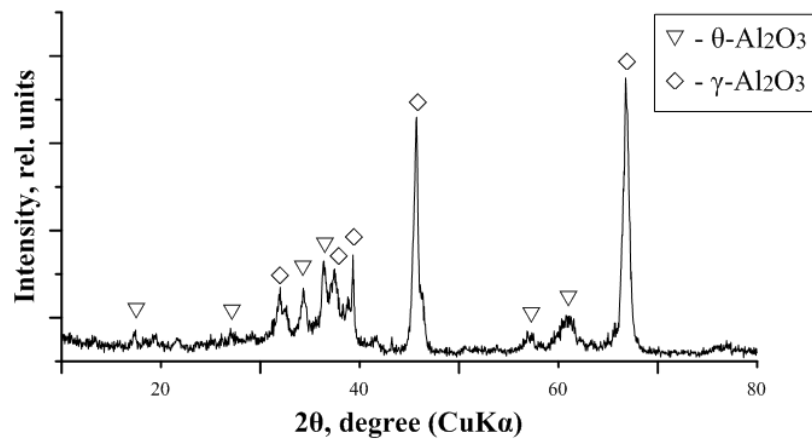


**Figure 2.** X-ray diffraction diagram of the  $\text{Al}_2\text{O}_3$  powder obtained via the plasma-chemical method.

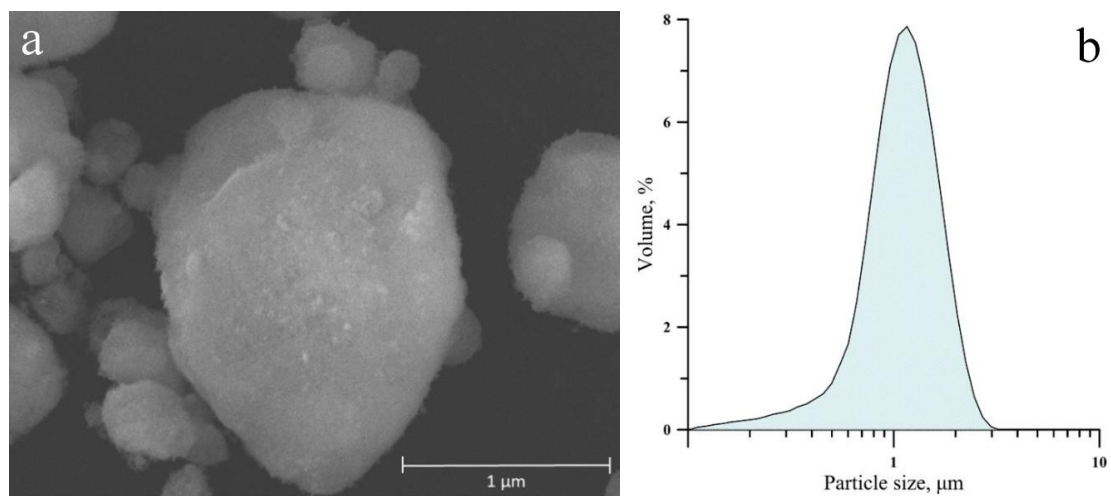


**Figure 3.** (a) An SEM image of the  $\text{Al}_2\text{O}_3$  powder and (b) a histogram of the particle distribution by size.

### 3.3. Aluminium Alloys

Table 2 shows a summary of the research of the properties of the alloys obtained.

**Table 2.** Properties of the alloys obtained.

SPD	Alloy	$\omega$ (MS/m)	IACS (%)	HV (MPa)	YS (MPa)	UTS (MPa)
No cycles	Ref (without particles)	$26.65 \pm 1.25$	$54.1 \pm 2.1$	$308 \pm 9.1$	$40 \pm 0.08$	$70 \pm 0.14$
	(i)	$27.45 \pm 0.65$	$52.67 \pm 1.13$	$329 \pm 3.3$	$38 \pm 0.076$	$73 \pm 0.146$
	(ii)	$27.3 \pm 0.6$	$52.93 \pm 1$	$366 \pm 7.9$	$39 \pm 0.078$	$68 \pm 0.136$
	(iii)	$37.1 \pm 0.8$	$36.03 \pm 1.38$	$359 \pm 7.1$	$42 \pm 0.084$	$78 \pm 0.156$
Two cycles	Ref (without particles)	$24.3 \pm 0.7$	$58.1 \pm 1.21$	$468 \pm 8.7$	$90 \pm 0.18$	$119 \pm 0.238$
	(i)	$25.6 \pm 1.1$	$55.9 \pm 1.94$	$527 \pm 11.5$	$86 \pm 0.172$	$107 \pm 0.214$
	(ii)	$29.1 \pm 0.5$	$49.8 \pm 1.1$	$576 \pm 17.8$	$100 \pm 0.2$	$129 \pm 0.258$
	(iii)	$36.3 \pm 0.4$	$37.4 \pm 0.7$	$562 \pm 21.8$	$102 \pm 0.204$	$133 \pm 0.266$
Four cycles	Ref (without particles)	$21.4 \pm 1.1$	$63.1 \pm 1.9$	$542 \pm 28.3$	$100 \pm 0.2$	$149 \pm 298$
	(i)	$24.8 \pm 0.7$	$57.2 \pm 1.2$	$562 \pm 13.5$	$93 \pm 0.186$	$153 \pm 0.306$
	(ii)	$26.7 \pm 1$	$53.9 \pm 1.7$	$665 \pm 18.2$	$103 \pm 0.206$	$165 \pm 0.33$
	(iii)	$31.2 \pm 0.8$	$46.2 \pm 1.38$	$593 \pm 11.7$	$97 \pm 0.194$	$159 \pm 0.318$

Note:  $\omega$  is the specific electrical conductivity of aluminum. IACS is the value of the electrical conductivity of samples relative to annealed copper. HV represents microhardness. YS represents yield strength. UTS represents ultimate tensile strength. The SPD column contains the number of pressing cycles for each alloy. Ref is the alloy without particles. i, ii and iii are the alloys reinforced with  $\text{TiB}_2/\text{TiC}$ ,  $\text{TiB}_2$  and  $\text{Al}_2\text{O}_3$ , respectively.

During the treatment of the experimental samples, the obtained data were selected and averaged, and the confidence ranges were determined for all statistical data. Figure 4 shows the typical experimental diagrams of “conditional stress–conditional strain” obtained by uniaxial tension of flat microsamples from the original alloy without disperse hardening. In the figure, curve 1 is the result of tensile a sample from the initial alloy without processing. Curves 2 and 3 correspond to the results of tensile samples from the original alloy after processing for two and four cycles of the ECAP. From the results of uniaxial tensile, a tendency to increase in the values of YS and UTS was noted, with a simultaneous decrease in the relative elongation for the samples after SPD treatment. A similar pattern in the change in the deformation behavior after SPD treatment is observed for all types of the studied alloys without particles and containing particles of  $\text{Al}_2\text{O}_3$ ,  $\text{TiB}_2$  and  $\text{TiB}_2/\text{TiC}$ . The differences were in the obtained values of the yield strength and strength for each alloy. The basic data obtained on the tensile strength of all the alloys under study, i.e., the conditional yield and strength limits, are given in Table 2.

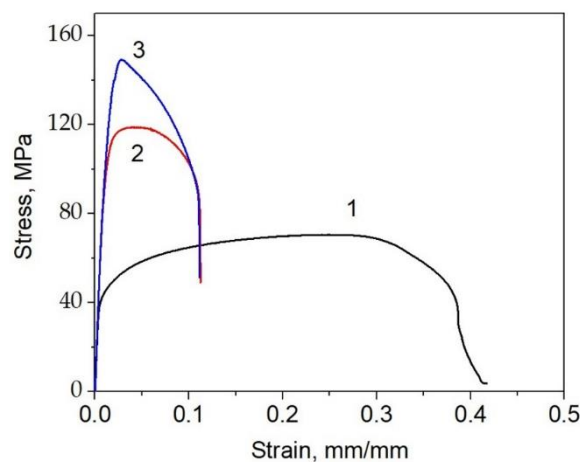


**Figure 4.** Typical alloy curves (1) without particles, (2) after two cycles of SPD and (3) after four cycles of SPD.

Microhardness tends to increase both after the introduction of hard-melting particles and after increasing the number of treatment cycles. The maximum microhardness of the materials in all the cases is greater in the samples containing  $\text{TiB}_2$  and lesser in the samples containing  $\text{Al}_2\text{O}_3$ . The lowest microhardness is seen in the samples that do not contain reinforcing particles. The introduction of hard-melting particles causes the electrical conductivity of aluminum to decrease. The least electrical resistance (between 36 and 46.2% IACS) was exhibited by the alloys containing  $\text{Al}_2\text{O}_3$  nanoparticles. Apparently, this is attributed to the particles being unevenly distributed throughout the material volume as agglomerates, and that is a significant obstacle for the free pass of electrons, leading to an increase in the electrical resistance of alloys. The highest electrical conductivity (63.1% IACS) was found in the alloys after four cycles of SPD. Figure 5 shows the combination of the electrical conductivity on the tensile strength of the alloys obtained. Data for other aluminum alloys can be seen in Reference [4]. It is seen in Figure 5, that from the point of view of the optimal combination of electrical conductivity and strength, the most beneficial trend is seen in the alloys alloyed with  $\text{TiB}_2$  particles after four cycles of SPD. In this case, the electrical conductivity is 53.9% IACS, the tensile strength is 165 MPa, the yield strength is 103 MPa, and HV is 665 MPa. This is attributed to the fact that SPD treatment creates a homogeneous ultra-fine structure that promotes an increase in the mechanical properties according to the Hall–Petch relationship [4]. An increase in the electrical conductivity is due to the SPD process promoting the purification of aluminum crystals through the expulsion of impurities from the solid solution and the purification of the crystals for the free pass of electrons [4]. The SPD process also amplifies the particle reinforcement effect by the even re-distribution of titanium diboride particles in aluminum grains, thus activating the Orowan mechanism. As such, the particles become

an obstacle for the travel of dislocations [15]. The fact that the presence of titanium diboride particles are not causing a substantial reduction of the electrical conductivity in the structure of aluminum is explained by the fact that the distance between  $\text{TiB}_2$  particles is greater or equal to the distance of the free pass of electrons. Otherwise, inclusions are an obstacle for electrons and the electric conductivity of the material would be lower. Mayadas A.F. [24], data are presented which indicate that the average distances of the free path of electrons are  $1.9 \mu\text{m}$ . Supplementary Figure S2 shows the SEM image by which one can estimate the distances between the particles of titanium diboride in aluminum alloys after four SPD cycles. The estimated average distance ( $l_{av}$ ) between the particles of titanium diboride was  $2.2 \mu\text{m}$ .

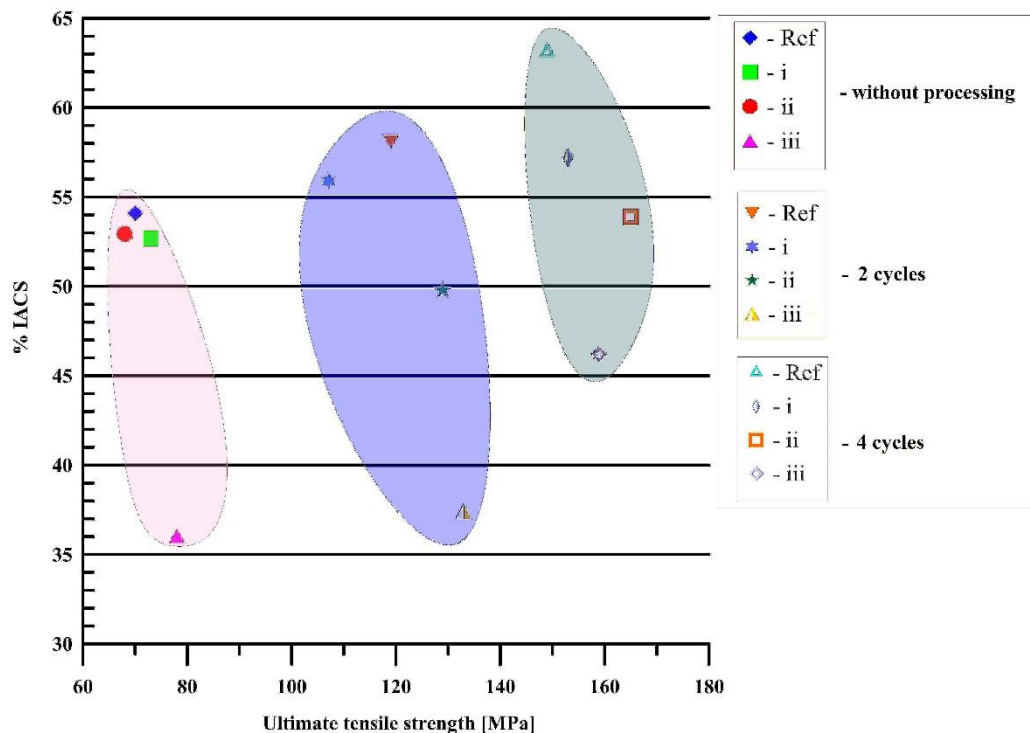


Figure 5. The electrical conductivity versus ultimate tensile strength of aluminum alloys.

#### 4. Conclusions

The results of the studies show the effect of dispersed hardening by  $\text{Al}_2\text{O}_3$  nanoparticles and microsized  $\text{TiB}_2$  and  $\text{TiC}$  particles and deformation processing using the ECAP method of pure aluminum on its electrical conductivity and strength properties. It has been found that the use of  $\text{TiB}_2$  particles for dispersed hardening of aluminum and in machining ECAPs allows one to increase the mechanical properties of the alloy without substantially reducing electrical conductivity. This phenomenon is manifested through the processing of ECAP, which contributes to the distribution of particles of the second phase in the structure of aluminum in such a way that they do not interfere with the free path of electrons. It has been established that with the introduction of  $\text{TiB}_2$  particles into aluminum and with simultaneous SPD processing, HV increases from 329 to 665 MPa, YS from 38 to 103 MPa, and UTS from 73 to 165 MPa, and the original electrical conductivity of cast aluminum without particles is maintained at 53.9–54.1% IACS. The agglomeration of nanosized particles of aluminum oxide, due to the action of van der Waals forces, does not allow for the achievement of the optimal structure of aluminum, which ensures high electrical conductivity. Moreover, the introduction of alumina nanoparticles into pure aluminum can significantly increase its microhardness. It was found that the initial electrical conductivity of 63.1% IACS with enhanced mechanical properties is possessed by the initial alloy without particles, subjected to a fourfold SPD treatment. This effect

is explained by the grinding of the grain and the exit of impurity elements from the crystal to the boundaries, which is a favorable factor for the free path of electrons.

**Supplementary Materials:** The following are available online at <http://www.mdpi.com/2075-4701/9/1/65/s1>, Figure S1: An TEM image of the Al<sub>2</sub>O<sub>3</sub> powder, Figure S2: An SEM image of the Al-TiB<sub>2</sub> alloy (ii) after four SPD cycles.

**Author Contributions:** I.A.Z.—idea of the paper, summary of results; A.A.K.—SPD treatment, analysis of results; A.P.K.—mechanical testing determination of powder size distribution, analysis of results; A.E.M.—synthesis SHS master-alloys, analysis of master-alloys; V.V.P.—alloys production, analysis of alloys; A.B.V.—determination of electrical properties of alloys, summary of results; T.V.Z.—choice of research methods; V.V.P.—materials structure research, analysis of results.

**Funding:** Russian Foundation for Basic Research: 16-38-60031 mol\_a\_dk, Council on grants of the President of the Russian Federation: 14.Y30.17.837-MK.

**Acknowledgments:** The research related to the synthesis of the Al<sub>2</sub>O<sub>3</sub> powder by plasma-chemical process was performed at IPCET SB RAS and was funded by RFBR, according to research project no. 16-38-60031 mol\_a\_dk. The research related to reinforcing the alloys with boride particles and studying their physico-mechanical properties was performed at Tomsk State University with the financial support of the Presidential Grant MK-837.2017.8, contract number 14.Y30.17.837-MK.

**Conflicts of Interest:** The authors declare no conflict of interest.

## References

1. Flores, F.U.; Seidman, D.N.; Dunand, D.C.; Vo, N.Q. Development of High-Strength and High-Electrical-Conductivity Aluminum Alloys for Power Transmission Conductors. In *TMS Annual Meeting & Exhibition*; Springer: Cham, Switzerland, 2018; pp. 247–251.
2. Cui, X.; Wu, Y.; Zhang, G.; Liu, Y.; Liu, X. Study on the improvement of electrical conductivity and mechanical properties of low alloying electrical aluminum alloys. *Compos. Part B Eng.* **2017**, *110*, 381–387. [[CrossRef](#)]
3. Karabay, S. Modification of AA-6201 alloy for manufacturing of high conductivity and extra high conductivity wires with property of high tensile stress after artificial aging heat treatment for all-aluminium alloy conductors. *Mater. Des.* **2006**, *27*, 821–832. [[CrossRef](#)]
4. Valiev, R.Z.; Murashkin, M.Y.; Sabirov, I. A nanostructural design to produce high-strength Al alloys with enhanced electrical conductivity. *Scr. Mater.* **2014**, *76*, 13–16. [[CrossRef](#)]
5. Yin, Z.; Pan, Q.; Zhang, Y.; Jiang, F. Effect of minor Sc and Zr on the microstructure and mechanical properties of Al–Mg based alloys. *Mater. Sci. Eng. A* **2000**, *280*, 151–155. [[CrossRef](#)]
6. Feng, X.; Liu, H.; Babu, S.S. Effect of grain size refinement and precipitation reactions on strengthening in friction stir processed Al–Cu alloys. *Scr. Mater.* **2011**, *65*, 1057–1060. [[CrossRef](#)]
7. Kendig, K.L.; Miracle, D.B. Strengthening mechanisms of an Al–Mg–Sc–Zr alloy. *Acta Mater.* **2002**, *50*, 4165–4175. [[CrossRef](#)]
8. Bobruk, E.V.; Murashkin, M.Y.; Kazykhanov, V.U.; Valiev, R.Z. Aging behavior and properties of ultrafine-grained aluminum alloys of Al–Mg–Si system. *Rev. Adv. Mater. Sci.* **2012**, *31*, 109–115.
9. Murashkin, M.Y.; Sabirov, I.; Kazykhanov, V.U.; Bobruk, E.V.; Dubravina, A.A.; Valiev, R.Z. Enhanced mechanical properties and electrical conductivity in ultrafine-grained Al alloy processed via ECAP-PC. *J. Mater. Sci.* **2013**, *48*, 4501–4509. [[CrossRef](#)]
10. Wang, X. The formation of AlB<sub>2</sub> in an Al–B master alloy. *J. Alloy. Compd.* **2005**, *403*, 283–287. [[CrossRef](#)]
11. Sabirov, I.; Murashkin, M.Y.; Valiev, R.Z. Nanostructured aluminium alloys produced by severe plastic deformation: New horizons in development. *Mater. Sci. Eng. A* **2013**, *560*, 1–24. [[CrossRef](#)]
12. Vorozhtsov, S.; Zhukov, I.; Vorozhtsov, A.; Zhukov, A.; Eskin, D.; Kvetinskaya, A. Synthesis of micro- and nanoparticles of metal oxides and their application for reinforcement of Al-based alloys. *Adv. Mater. Sci. Eng.* **2015**, *2015*, 718207. [[CrossRef](#)]
13. Vorozhtsov, S.; Minkov, L.; Dammer, V.; Khrustalyov, A.; Zhukov, I.; Promakhov, V.; Khmeleva, M. Ex Situ Introduction and Distribution of Nonmetallic Particles in Aluminum Melt: Modeling and Experiment. *JOM* **2017**, *69*, 2653–2657. [[CrossRef](#)]
14. Naydenkin, E.; Mishin, I.; Khrustalyov, A.; Vorozhtsov, S.; Vorozhtsov, A. Influence of Combined Helical and Pass Rolling on Structure and Residual Porosity of an AA6082-0.2 wt% Al<sub>2</sub>O<sub>3</sub> Composite Produced by Casting with Ultrasonic Processing. *Metals* **2017**, *7*, 544. [[CrossRef](#)]

15. Vorozhtsov, S.; Zhukov, I.; Promakhov, V.; Naydenkin, E.; Khrustalyov, A.; Vorozhtsov, A. The Influence of ScF<sub>3</sub> Nanoparticles on the Physical and Mechanical Properties of New Metal Matrix Composites Based on A356 Aluminum Alloy. *JOM* **2016**, *68*, 3101–3106. [[CrossRef](#)]
16. Vorozhtsov, S.A.; Promakhov, V.V.; Eskin, D.G.; Vorozhtsov, A.B.; Zhukov, I.A. The use of alumina and zirconia nanopowders for optimization of the Al-based light alloys. In *TMS Annual Meeting & Exhibition*; Springer: Cham, Switzerland, 2015; pp. 25–32.
17. Zhukov, I.A.; Ziatdinov, M.K.; Vorozhtsov, A.B.; Zhukov, A.S.; Vorozhtsov, S.A.; Promakhov, V.V. Self-Propagating High-Temperature Synthesis of Al and Ti Borides. *Russ. Phys. J.* **2016**, *59*, 1324–1326. [[CrossRef](#)]
18. Zhukov, I.A.; Promakhov, V.V.; Matveev, A.E.; Platov, V.V.; Khrustalev, A.P.; Dubkova, Y.A.; Potekaev, A.I. Principles of Structure and Phase Composition Formation in Composite Master Alloys of the Al–Ti–B/B<sub>4</sub>C Systems Used for Aluminum Alloy Modification. *Russ. Phys. J.* **2018**, *60*, 2025–2031. [[CrossRef](#)]
19. Vorozhtsov, S.; Vorozhtsov, A.; Kudryashova, O.; Zhukov, I.; Promakhov, V. Structural and mechanical properties of aluminium-based composites processed by explosive compaction. *Powder Technol.* **2017**, *313*, 251–259. [[CrossRef](#)]
20. Zhukov, I.A.; Bondarchuk, S.S.; Basalaev, S.A.; Vorozhtsov, A.B.; Platov, V.V.; Titov, S.S. Nonlinear Dependence of Sprayed Drop Sizes on the Mass Fraction of a Salt Precursor Component. *Russ. Phys. J.* **2018**, *60*, 1845–1847. [[CrossRef](#)]
21. Zhukov, I.; Bondarchuk, S.; Borisov, B.V. Double Continuum Model of Evolution of Precursor Droplets in the Flow of Heat Transfer Medium of a Plasma Chemical Reactor. *MATEC Web Conf.* **2016**, *72*, 01016. [[CrossRef](#)]
22. Zhukov, I.; Promakhov, V.; Vorozhtsov, S.; Kozulin, A.; Khrustalyov, A.; Vorozhtsov, A. Influence of Dispersion Hardening and Severe Plastic Deformation on Structure, Strength and Ductility Behavior of an AA6082 Aluminum Alloy. *JOM* **2018**, *70*, 2731–2738. [[CrossRef](#)]
23. Sauter, C.; Emin, M.A.; Schuchmann, H.P.; Tavman, S. Influence of hydrostatic pressure and sound amplitude on the ultrasound induced dispersion and de-agglomeration of nanoparticles. *Ultrason. Sonochem.* **2008**, *15*, 517–523. [[CrossRef](#)] [[PubMed](#)]
24. Mayadas, A.F. Intrinsic resistivity and electron mean free path in aluminum films. *J. Appl. Phys.* **1968**, *39*, 4241–4245. [[CrossRef](#)]



© 2019 by the authors. Licensee MDPI, Basel, Switzerland. This article is an open access article distributed under the terms and conditions of the Creative Commons Attribution (CC BY) license (<http://creativecommons.org/licenses/by/4.0/>).